Journal of Power Sources 396 (2018) 12–18

Contents lists available at ScienceDirect

Journal of Power Sources

journal homepage: www.elsevier.com/locate/jpowsour

A hybrid sodium-ion capacitor with polyimide as anode and polyimide-derived carbon as cathode

Qinglan Zhao[a], Dongfang Yang[a], Andrew K. Whittaker[b,c], X.S. Zhao[a,*]

[a] School of Chemical Engineering, The University of Queensland, St. Lucia, Q4072, Australia
[b] Australian Institute for Bioengineering and Nanotechnology, The University of Queensland, St. Lucia, Q4072, Australia
[c] ARC Centre of Excellence in Convergent Bio-Nano Science and Technology, The University of Queensland, St. Lucia, Q4072, Australia

HIGHLIGHTS

- Both of anode and cathode came from the single polymer.
- Polyimide and polyimide-derived carbon were respectively used as anode and cathode.
- Battery-type anode and capacitor-type cathode made hybrid sodium-ion capacitor.
- Pore texture of polyimide-derived carbon with high surface area was adjusted.

GRAPHICAL ABSTRACT

A scheme showing the configuration of a hybrid sodium-ion capacitor.

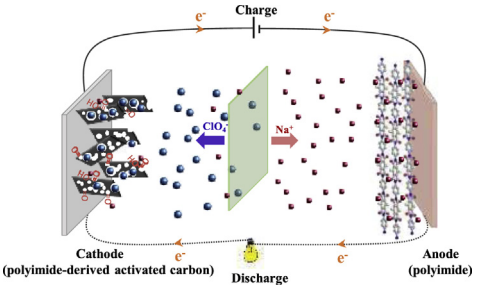

ARTICLE INFO

Keywords:
Polymer
Polyimide
Carbon
Hybrid sodium-ion capacitor

ABSTRACT

In this work, pyromellitic dianhydride-based polyimide was hydrothermally synthesised and further thermally treated to prepare porous carbon materials. The porous structure of the polyimide-derived carbon can be controlled by varying the reactant concentrations during the hydrothermal reaction and KOH activation to achieve a highly accessible specific surface area of 1302 $m^2 g^{-1}$. A hybrid sodium-ion capacitor fabricated with the polyimide as anode and the polyimide-derived carbon as cathode can be operated at a voltage of 4.2 V, delivering an energy density of 66 Wh kg^{-1} at power density of 196 W kg^{-1}, and an energy density of 13.3 Wh kg^{-1} at power density of 1200 W kg^{-1}.

1. Introduction

Sodium-ion storage systems including sodium-ion batteries (NIBs) and sodium-ion capacitors (NICs) are regarded as promising alternatives to lithium-ion storage systems, due to the high abundance and low cost of sodium resources (the cost of Na_2CO_3 is only 3% of that of Li_2CO_3), as well as the similar electrochemical properties to lithium (sodium is only 0.3 V more positive than lithium) [1–14]. Sodium-ion based batteries provide a high energy density but suffer from sluggish charge and discharge responses [15]. NICs are sodium-ion based hybrid ion capacitors consisting of a battery-type negative electrode (anode) and a capacitor-type positive electrode (cathode) [16]. Such a system works via two charge storage mechanisms: (i) for the anode, charge is stored by insertion/extraction of the cations, which can produce high energy density but sluggish kinetics; (ii) for the cathode, charge is stored by fast reversible adsorption/desorption of the anions, which can enhance the rate capability to offer higher power density.

One of the major challenges for sodium-ion storage systems is the lack of a suitable anode material [17–22]. The most commonly used anode in lithium-ion batteries (LIBs), graphite, is thermodynamically unfavourable for NIBs [23]. Many transition-metal oxides have been studied as anode materials for NIBs [24–28]. The insertion of sodium

* Corresponding author.
E-mail address: george.zhao@uq.edu.au (X.S. Zhao).

https://doi.org/10.1016/j.jpowsour.2018.06.010
Received 23 February 2018; Received in revised form 18 May 2018; Accepted 2 June 2018

ions into these materials can cause multi-step phase transitions, leading to a low utilisation of capacity and/or a sluggish kinetics [29].

In recent years, organic materials have received increasing research attention because of their facile processability, compositional diversity and flexibility [30,31]. Such materials can be obtained from natural products and biomasses with minimum energy consumption by appropriate design and treatment, which may further lower the cost of devices [32–34]. Polyimides have high mechanical strength, excellent thermal stability and high density of electroactive functional groups [35,36], are cheap and easy to be scaled up in production [37], and hence are of particular importance to rechargeable batteries. Aromatic polyimides, containing a dianhydride core as the aromatic backbone, have been used as cathodes for NIBs [38–42]. Recently, it was found that when altering the aromatic core from perylene 3,4,9,10-tetracarboxylic dianhydride (PTCDA) to 1,4,5,8-naphthalenetetracarboxylic dianhydride (NTCDA) and further to pyromellitic dianhydride (PMDA), the average discharge voltage became progressively lowered [33]. And the average discharge voltage of the PMDA-based polyimides was about 1.73 V, suggesting its suitability as an anode for NIBs [23].

Polyimides have been used as a precursor to prepare porous carbon materials [43–45], which can be used as a capacitor-type cathode for NICs due to their excellent electrical conductivity, high surface area, good thermal and chemical stability, as well as low cost. In this study, a hybrid NIC was realized for the first time by employing a PMDA-based polyimide as the anode and a polyimide-derived porous carbon as the cathode. The NIC cell delivered a high energy density without significantly sacrificing power density.

2. Experimental section

2.1. Synthesis of polyimides

According to our previous work [46], 2.5 mmol *p*-phenylenediamine (PPD) was dissolved in 30.0 mL *N*,*N*-dimethylformamide (DMF) followed by addition of equimolar PMDA. Then, the mixture was transferred into a Teflon-lined autoclave and heated at 210 °C for 10 h in an oven. The precipitates were centrifuged, washed with DMF and ethanol, and dried under vacuum at 80 °C. The obtained polyimide samples are designated as PI-1.25, PI-2.5 and PI-5, where 1.25, 2.5 and 5 indicate the concentrations of PPD and PMDA added to the synthesis system in millimoles per litre.

2.2. Synthesis of polyimide-derived carbons

PI-1.25, PI-2.5 and PI-5 were further thermally treated at 650 °C for 3 h under N_2 to obtain carbon samples, designated as C(PI-1.25), C(PI-2.5) and C(PI-5). To further develop pores, KOH activation was used to activate the polyimide-derived carbons. Typically, 1 g C(PI-1.25), C(PI-2.5) or C(PI-5) was impregnated in a mixture of 40 mL of 0.1 g mL^{-1} KOH solution and 4 mL of 25% ethanol aqueous solution. After stirring for 1 h, the mixture was dried at 60 °C overnight to evaporate the solvent and heated at 650 °C for 1 h under N_2 at a heating rate of 5 °C min^{-1}. The activated carbons were then immersed in 1 mol L^{-1} HCl to remove the residue KOH and washed with distilled water until neutral pH. Samples thus obtained are designated as AC(PI-1.25), AC(PI-2.5) and AC(PI-5).

2.3. Characterization

Thermogravimetry (TG) analysis was conducted on a thermal analyser (DTG-60A, Shimadzu) under nitrogen at a heating rate of 5 °C min^{-1}. Field emission scanning electron microscope (FESEM) (JSM-7001 F, JEOL) was used to characterise the morphology of the samples. Transmission electron microscopy (TEM) images were recorded on a transmission electron microscope (JEM2100, JEOL). X-ray diffraction (XRD) measurements were collected on an X-ray diffractometer (Bruker D8 Advance, Bruker) with Cu Kα radiation (λ = 1.54056 Å). Raman spectra were performed using a Raman spectrometer (Renishaw) with a 514 nm laser. Argon adsorption-desorption measurements were carried out on a TriStar II 3020 (Micromeritics) at 87.3 K. The specific surface area (S_{BET}) and pore size distribution were analysed by using the Brunauer-Emmett-Teller (BET) and non-local density functional theory (NL-DFT) methods, respectively. The total pore volume (V_t) was estimated at a relative pressure of 0.99. The micropore volume (V_{mic}) was obtained from the t-plot method. The mesopore volume (V_{meso}) was calculated from the difference between V_t and V_{mic}. X-ray photoelectron spectroscopy (XPS) spectra were recorded on a Kratos Axis Ultra photoelectron spectrometer.

2.4. Electrochemical measurements

For the preparation of polyimide electrodes, polyimide, carbon black and poly (vinylidene difluoride) (PVDF) at a mass ratio of 6:3:1 were dispersed in *N*-methyl pyrrolidone (NMP) to form a slurry, which was cast onto a copper foil current collector using a doctor blade. The electrode was dried at 60 °C under vacuum overnight. For the fabrication of polyimide-derived porous carbon electrodes, the same procedure was used except the mass ratio of porous carbon:carbon black:PVDF = 8:1:1 and the current collector was aluminium foil.

Half cells were assembled in an Ar-filled glovebox using the polyimide or polyimide-derived porous carbon as the working electrode, pure sodium foil as the counter electrode, glass fibre as the separator and 1 mol L^{-1} $NaClO_4$ in equal volumes of ethylene carbonate (EC) and propylene carbonate (PC) mixed with 0.3 wt % fluoroethylene carbonate (FEC) as the electrolyte. NIC cells were fabricated using the polyimide electrode as anode and polyimide-derived porous carbon electrode as cathode with the same separator and electrolyte.

Galvanostatic discharge and charge (GCD) cycling of the half cells and NICs were conducted on a battery tester (CT3008, Neware) and a potentiostat/galvanostat (PGSTAT302 N, Metrohm Autolab) at room temperature. Cyclic voltammetry (CV) was performed on an electrochemical workstation (CHI 660D, Chen Hua Instrument). The calculations for the NICs were based on the total mass of active materials in both anodes and cathodes. The energy and power densities were calculated according to the following equations:

$$E = P \times t \tag{1}$$

$$P = \frac{E}{t} = \Delta V \times \frac{I}{m} = (V_{max} - V_{min}) \times \frac{I}{m} \tag{2}$$

where t is the discharge time, I is the discharge current, m is the total mass of active materials in both electrodes, and V_{max} and V_{min} are the voltage at the beginning and end of discharge, respectively.

3. Results and discussion

3.1. Polyimide as anode material

PI-2.5 delivering a reversible discharge capacity of 125 mAh g^{-1} was employed as the anode material for the hybrid sodium-ion capacitor, the redox mechanism (Scheme 1) of which can be illustrated as a

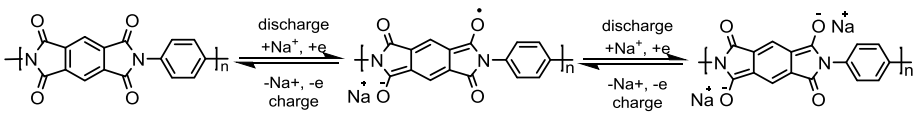

Scheme 1. Discharge and charge mechanism for the polyimide electrode in half cell.

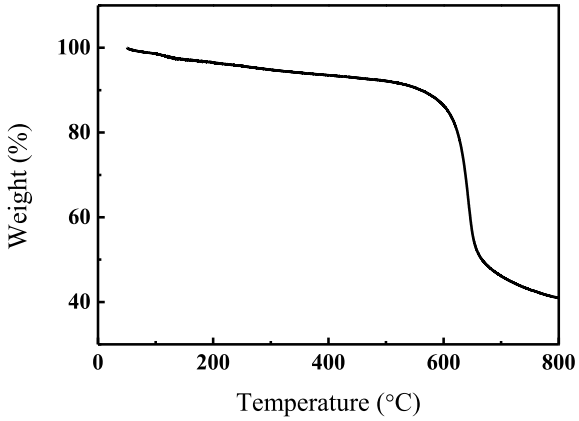

Fig. 1. TG curve of an as-synthesised polyimide sample.

two-step enolisation reaction with reversible insertion of two sodium ions according to our previous work [46].

3.2. Polyimide-derived carbon as cathode material

Fig. 1 shows the TG curve of an as-synthesised polyimide sample in nitrogen atmosphere. It can be observed that this polyimide is thermally stable up to 500 °C in N_2. Such relatively good thermal stability can be an important advantage for this material from the safety viewpoint in sodium-ion storage systems [39]. The polyimide started to decompose at about 500 °C with a resident carbon content of about 40% at 800 °C. Such a high carbon residue after thermal treatment is favourable for making polyimide-derived carbon materials [45]. Based on the TG data, the carbonization temperature for the polyimides was 650 °C.

All the polyimide-derived carbons possessed a thin sheet-like morphology as shown in Fig. 2a–c. Such a morphology can minimize diffusion distances of the electrolyte ions [47,48]. It is seen that the carbon particles consist of two-dimensional sheets, which offer a high specific surface area and are favourable for charge storage via an electric double layer (EDL) mechanism. The interconnected sheets in the carbons can act as inter-sheet transport charge transporters and transport electrolyte ions rapidly during the charge and discharge processes. The morphology of the polyimide-derived carbons was generally inherited after KOH activation (Fig. 2d–f). The more highly interconnected morphology was better conserved since the self-supported hierarchical structure prevented the collapse of sheets during the high-temperature activation process.

From the Raman spectra (Fig. S1), the ratio of the relative intensity of the disorder-induced (D) band (1350 cm^{-1}) and graphite-like G band (1596 cm^{-1}) is relatively constant for all samples (I_G/I_D = 1.2). However, the activated carbons show a broader D band and G band at full width at half maximum, indicating that the activated carbons have a more disordered structure [49]. Fig. 2g shows the XRD patterns of samples C(PI-5) and AC(PI-5). The XRD patterns confirm the amorphous nature of the carbons, with an obviously broad peak at 2θ of ca. 22° and a weak peak at 2θ of ca. 43° corresponding to the (002) and (001) planes of pseudographitic domains. After KOH activation, AC(PI-5) demonstrated a broader (002) peak, suggesting a more disordered structure, consistent with the Raman results. The TEM image (Fig. 2h) of AC(PI-5) shows obvious micropores and mesopores generated from the thermal and activation treatments. The high resolution TEM (HRTEM) image and the selected area electron diffraction (SAED) pattern (Fig. 2i) further confirm the amorphous structure of the

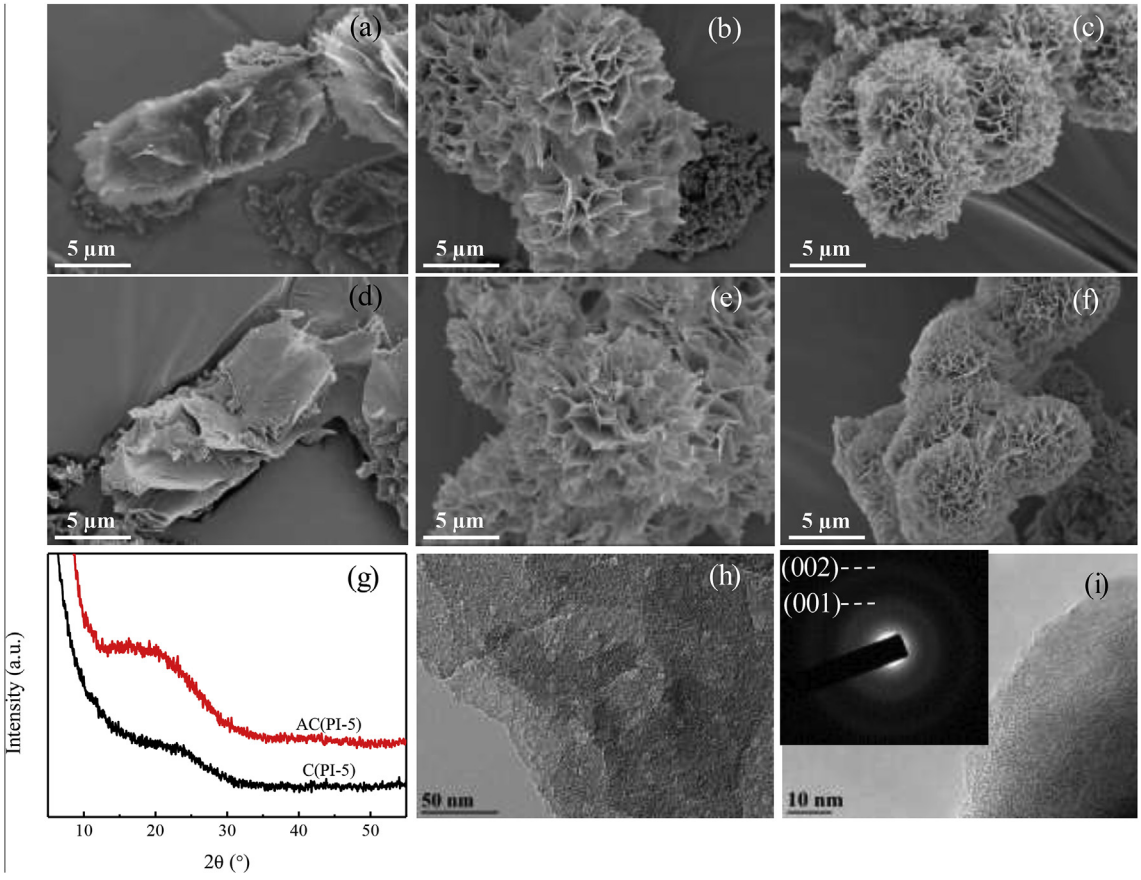

Fig. 2. (a–f) FESEM images of (a) C(PI-1.25), (b) C(PI-2.5), (c) C(PI-5), (d) AC(PI-1.25), (e) AC(PI-2.5) and (f) AC(PI-5), (g) XRD patterns of C(PI-5) and AC(PI-5), (h) TEM image of AC(PI-5), (i) HRTEM image of AC(PI-5) with its corresponding SAED pattern shown as an insert.

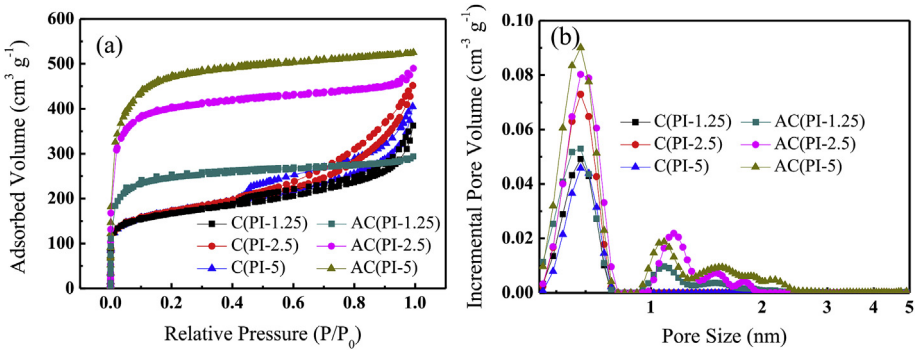

Fig. 3. (a) Argon adsorption-desorption isotherms and (b) NL-DFT pore size distributions of C(PI-1.25), C(PI-2.5), C(PI-5), AC(PI-1.25), AC(PI-2.5) and AC(PI-5).

Table 1
Texture properties derived from the argon adsorption-desorption measurements and surface chemistry determined by XPS.

Sample	S_{BET} (m^2 g^{-1})	V_t (cm^3 g^{-1})	V_{mic} (cm^3 g^{-1})	V_{meso} (cm^3 g^{-1})	Elemental content (atom %)		
					C	N	O
C(PI-1.25)	473	0.46	0.12	0.34	86.82	9.99	3.19
C(PI-2.5)	493	0.58	0.11	0.47	86.17	10.50	3.33
C(PI-5)	489	0.52	0.11	0.41	86.77	10.01	3.22
AC(PI-1.25)	678	0.38	0.23	0.15	82.04	4.41	13.55
AC(PI-2.5)	1099	0.63	0.39	0.24	83.73	3.77	12.50
AC(PI-5)	1302	0.67	0.40	0.27	85.20	2.25	12.55

polyimide-derived activated carbons.

Fig. 3a shows the argon adsorption-desorption isotherms and pore size distributions of the polyimide-derived carbons before and after KOH activation. The textural parameters derived from the argon sorption data are listed in Table 1. All the carbon samples mainly exhibit a type I isotherm, suggesting that they are microporous materials, consistent with the pore size distribution in Fig. 3b. The plentiful micropores can build up the electrical double layer capacitance [50,51]. From Table 1, the AC(PI-5) had the highest S_{BET} of 1302 m^2 g^{-1} which is comparable to that of the activated carbons used in commercial electrochemical double layer capacitors (EDLCs) [52], making it suitable for hybrid NICs.

Fig. 4a shows the wide-scan XPS spectra of samples, and the quantitative analysis data based on the XPS results are given in Table 1. O1s peak at 532.7 eV, N1s peak at 400.9 eV, and C1s peak at 284.8 eV can be seen, indicating the samples are composed of carbon, nitrogen and oxygen elements. After KOH activation, the oxygen content increased while the nitrogen content decreased. This is due to the introduction of oxygen and the oxidation of nitrogen during the KOH activation process [53]. From the high resolution C1s spectrum of sample AC(PI-5) presented in Fig. 4b, four deconvoluted peaks at 284.7 eV, 285.9 eV, 287.7 eV and 290.2 eV can be identified, coming from the C-C, C-N and C-O, C=O, and O=C-O groups, respectively [45]. The high-resolution N1s spectrum (Fig. 4c) can be resolved into peaks due to pyridinic nitrogen (N-6, 398.5 eV), pyrrolic/pyridine nitrogen (N-5, 400.2 eV), and quaternary nitrogen (N-Q, 402.4 eV) [54]. The O1s spectrum (Fig. 5c) could be deconvoluted into three subpeaks of C=O (530.8 eV), C-O (532.5 eV) and O=C-O (534.9 eV) [55]. The functional groups can contribute to substantial pseudocapacitance by

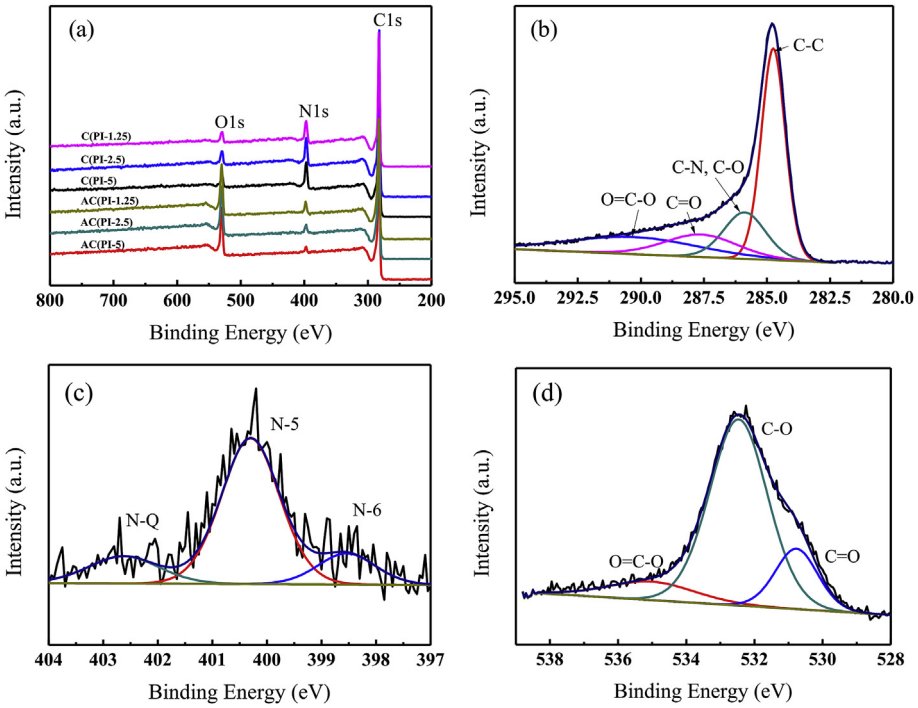

Fig. 4. (a) XPS survey spectra of C(PI-1.25), C(PI-2.5), C(PI-5), AC(PI-1.25), AC(PI-2.5) and AC(PI-5); (b–d) high resolution XPS (b) C1s, (c) N1s and (d) O1s spectrum of AC(PI-5).

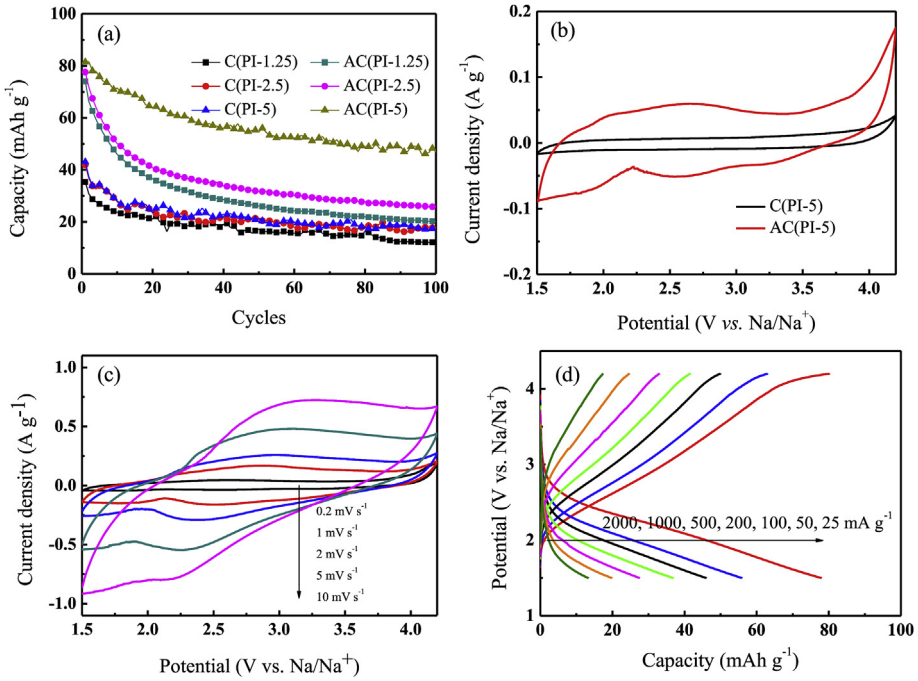

Fig. 5. (a) Cycling performance of C(PI-1.25), C(PI-2.5), C(PI-5), AC(PI-1.25), AC(PI-2.5) and AC(PI-5), (b) CV curves of C(PI-5) and AC(PI-5) at a scan rate of 0.2 mV s^{-1}, (c) CV curves of AC(PI-5) at different scan rates, and (d) the GCD profiles of AC(PI-5) at different current densities in half cell.

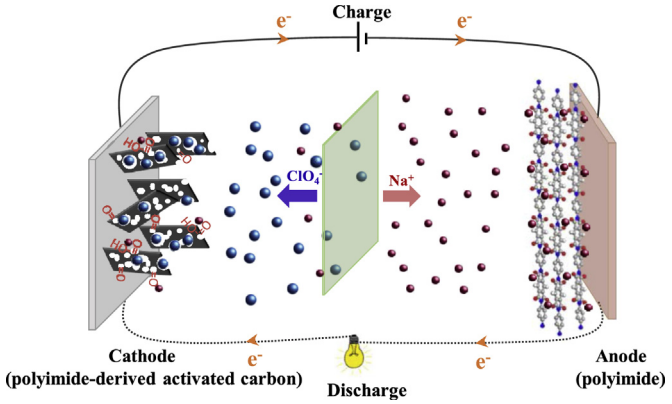

Scheme 2. A scheme showing the configuration of a NIC cell.

interacting with sodium ions reversibly [16,56,57]. Thus, by employing the polyimides with different morphology and using the activation process, activated carbons with various porous structures and heteroatom contents can be obtained conveniently.

Fig. 5a presents the cycling performance of polyimide-derived carbons and KOH-activated carbons. In general, the KOH activated carbons displayed better performance than the polyimide-derived carbons. Sample AC(PI-5) delivered the highest capacity during the 100 cycles due to its optimum combination of accessible surface area, appropriate pore size distribution and surface functional groups. Fig. 5b compares the CV curves of the polyimide-derived carbons and carbons after KOH activation in a potential window between 1.5 and 4.2 V vs. Na/Na^+. This potential range can allow the maximum operating voltage window without decomposing the electrolyte and also limits the electrolyte ion intercalation into the bulk carbons [16]. During positive polarization, perchlorate anions were adsorbed and sodium ions were released. Compared with the small rectangular CV curve of C(PI-5), the AC(PI-5) gave a higher current response and thus a much larger CV curve with pseudocapacitive humps around 2.2–3.5 V. The capacitance of AC(PI-5) was contributed by the EDLC formed by adsorption of perchlorate anions and pseudocapacitive interaction of sodium ions with surface defects and functional groups. As is shown in Fig. 5c, the CV curves of AC(PI-5) show negligible shape distortion with increasing scan rate from 1 mV s^{-1} to 10 mV s^{-1}, indicating fast kinetics and good reversibility of this activated carbon. The GCD profiles for AC(PI-5) in Fig. 5d show generally a linear increase in capacity with respect to the potential, suggesting the major contributor to capacitive behaviour is formation of a perchlorate anion double layer. The slight deviation from the linear shape in the GCD curves comes from the pseudocapacitance contributed by the interaction of sodium ions with surface defects and functional groups, consistent with the CV observations.

3.3. Performance of hybrid sodium-ion capacitor

Based on the electrochemical performance of the polyimide-derived carbons in half cells, AC(PI-5) was chosen for the assembly of the hybrid NIC. The mass ratio of cathode to anode was roughly maintained at ~3, based on the storage capacities of both electrodes. Both anodes and cathodes were pre-activated for 10 cycles at 25 mA g^{-1} prior to assembly of the NIC to minimize irreversible capacity loss [58,59]. A voltage window between 0 and 4.2 V was set to maximise the use of working voltage to offer high energy density [60] without electrolyte decomposition [61]. Upon charging (Scheme 2), the PI-2.5 anode experiences reversible insertion of sodium ions via enolisation with carbonyl groups, while the AC(PI-5) cathode reversibly adsorbs perchlorate anions and releases sodium ions from surface defects and functional groups. The reverse process occurs during the subsequent discharge.

As is shown in Fig. 6a, the CV curves of the PI-2.5//AC(PI-5) hybrid NIC displayed a generally rectangular shape with voltage up to 4.2 V, suggesting interfacial electrochemical capacitive behaviour with good reversibility. The shape of the CV curves was maintained even at a high scan rate of 100 mV s^{-1}, indicating a fast charge transfer kinetics of this hybrid NIC. The galvanostatic charge and discharge curves show a linear shape with slight deviation, consistent with the CV observations. The internal resistance (iR drop) of the galvanostatic discharge curves can be reduced by enhancing the conductivity of the electrode materials to further improve the overall performance of the hybrid NIC device. The initial specific capacities of the hybrid NICs were 31, 29, 26, 14 and

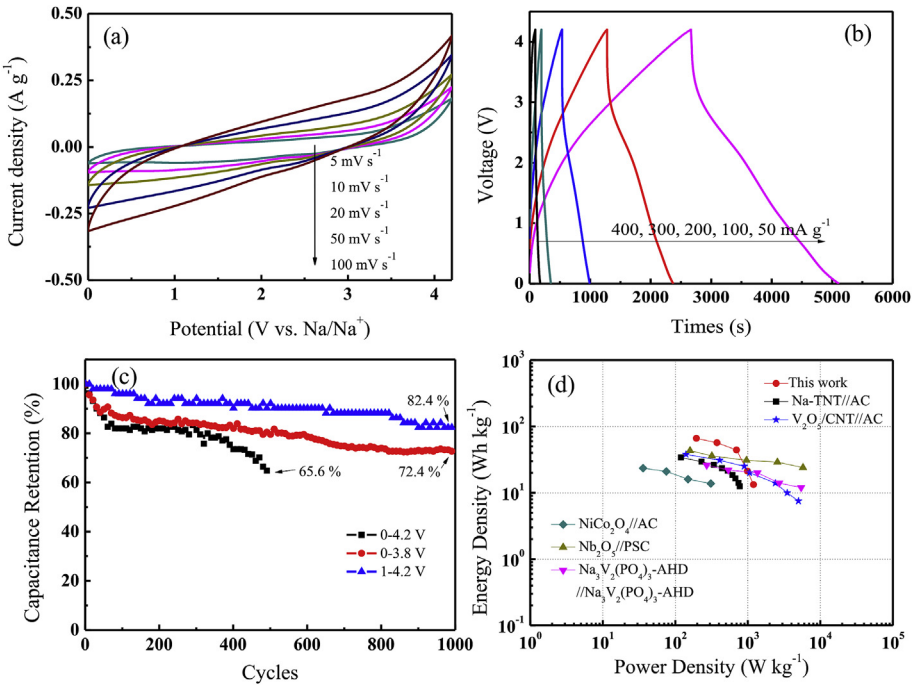

Fig. 6. Electrochemical performance of the PI-2.5//AC(PI-5) hybrid NIC: (a) CV curves at different scan rates from 5 to 100 mV s^{-1}, (b) galvanostatic charge and discharge curves at different current densities from 50 to 400 mA g^{-1}, (c) cycling performance of different voltage windows at 400 mA g^{-1}, and (d) Ragone plot in comparison with other commercial energy storage devices and other reported NICs (Na-TNT//AC [63], V_2O_5/CNT//AC [64], $NiCo_2O_4$//AC [65], Nb_2O_5 nanosheets//PSC [66], $Na_3V_2(PO_4)_3$-AHD//$Na_3V_2(PO_4)_3$-AHD [67], TNT: sodium titanate nanotube, CNT: carbon nanotube, PSC: peanut shell carbon, AHD: ambient hydrolysis deposition).

11 F g^{-1} at current densities of 50, 100, 200, 300, 400 mA g^{-1}, respectively. As is shown in Fig. 6c, at the 500th cycle of charging and discharging at a current density of 400 mA g^{-1}, 65.6% of the initial capacitance was retained for the hybrid NIC. Such a large voltage window of 0–4.2 V usually leads to degradation of cycling stability [58,62]. The retention of capacitance increased to 72.4% at the 1000th cycle when a smaller window of 0–3.5 V was applied, which may be due to the reduced rates of degradation in the oxygen functional groups of AC(PI-5) [16]. When the voltage window was adjusted to 1–4.2 V (Fig. S2), the shape of the CV and GCD curves remained almost the same with a lower capacitance (26.4 F g^{-1} at 50 mA g^{-1}) and a higher capacitance retention (82.4% at the 1000th cycle).

Fig. 6d shows the Ragone plot of the hybrid NIC based on the total mass of active materials in both the anode and cathode. The PI-2.5//AC(PI-5) hybrid NIC exhibited a high energy density of 66 Wh kg^{-1} at a power density of 196 W kg^{-1}, and energy density of 13.3 Wh kg^{-1} at a high power density of 1200 W kg^{-1}. When compared with previously reported asymmetric/symmetric sodium-ion capacitors based on metal oxides/polyanion compounds and activated carbons as shown in Fig. 6d, the PI-2.5//AC(PI-5) hybrid NIC gave high energy density without significant sacrifice in power density. The overall energy-power performance of the PI-2.5//AC(PI-5) hybrid NIC is close to lithium-ion batteries and comparable to supercapacitors, making this NIC very promising for the energy storage field. Upon industrial engineering optimisation, such as improved electrode fabrication processes, the mass ratio of both electrodes, and electrolyte component refinement, the overall performance of the hybrid NIC should be further improved.

4. Conclusions

In summary, a unique approach to the creation of hybrid sodium-ion capacitors has been proposed with active materials in both electrodes derived from the single organic precursor, which is cheap and environmentally friendly. The polyimide-derived activated carbons with highly accessible specific surface area can retain the original microflower-like nanosheet morphology of the polyimide precursor. The hybrid sodium-ion capacitors using polyimide as anode and polyimide-derived activated carbon as cathode delivered high energy density of 66 Wh kg^{-1} at a power density of 196 W kg^{-1} and energy density of 13.3 Wh kg^{-1} at a power density of 1200 W kg^{-1}. The strategy of employing a polymer as battery-type anode and a polymer-derived carbon as capacitor-type cathode represents a new concept of fabricating an energy storage device from a single polymer.

Acknowledgements

This research was supported by the Australian Research Council under the ARC Laureate Fellowship program (FL170100101). QZ thanks the International Postgraduate Research Scholarship funded by the Australian Government and the UQ Centennial Scholarship. The authors gratefully acknowledge the facilities, scientific and technical assistance of the Australian Microscopy and Microanalysis Research Facility at the UQ Centre for Microscopy and Microanalysis. The Australian National Fabrication Facility, Queensland Node, is also acknowledged for allowing access to equipment.

Appendix A. Supplementary data

Supplementary data related to this article can be found at http://dx.doi.org/10.1016/j.jpowsour.2018.06.010.

References

[1] J.M. Tarascon, M. Armand, Issues and challenges facing rechargeable lithium batteries, Nature 414 (2001) 359–367.
[2] F. Wan, X.L. Wu, J.Z. Guo, J.Y. Li, J.P. Zhang, L. Niu, R.S. Wang, Nanoeffects promote the electrochemical properties of organic $Na_2C_8H_4O_4$ as anode material for sodium-ion batteries, Nanomater. Energy 13 (2015) 450–457.
[3] K. Saravanan, C.W. Mason, A. Rudola, K.H. Wong, P. Balaya, The first report on excellent cycling stability and superior rate capability of $Na_3V_2(PO_4)_3$ for sodium ion batteries, Adv. Energy Mater. 3 (2013) 444–450.
[4] M. Armand, J.M. Tarascon, Building better batteries, Nature 451 (2008) 652–657.
[5] C. Wang, Y. Xu, Y. Fang, M. Zhou, L. Liang, S. Singh, H. Zhao, A. Schober, Y. Lei, Extended π-conjugated system for fast-charge and -discharge sodium-ion batteries, J. Am. Chem. Soc. 137 (2015) 3124–3130.
[6] V. Palomares, P. Serras, I. Villaluenga, K.B. Hueso, J. Carretero-González, T. Rojo, Na-ion batteries, recent advances and present challenges to become low cost energy storage systems, Energy Environ. Sci. 5 (2012) 5884–5901.
[7] S. Yuan, Y.H. Zhu, W. Li, S. Wang, D. Xu, L. Li, Y. Zhang, X.B. Zhang, Surfactant-free aqueous synthesis of pure single-crystalline SnSe nanosheet clusters as anode for high energy-and power-density sodium-ion batteries, Adv. Mater. 29 (2017) 1602469.
[8] T. Sun, Z. Li, H. Wang, D. Bao, F. Meng, X. Zhang, A biodegradable polydopamine-

derived electrode material for high-capacity and long-life lithium-ion and sodium-ion batteries, Angew. Chem. Int. Ed. 128 (2016) 10820–10824.
[9] S. Yuan, Y.B. Liu, D. Xu, D.L. Ma, S. Wang, X.H. Yang, Z.Y. Cao, X.B. Zhang, Pure single-crystalline $Na_{1.1}V_3O_{7.9}$ nanobelts as superior cathode materials for re-chargeable sodium-ion batteries, Adv. Sci. 2 (2015) 1400018.
[10] S. Wang, T. Sun, S. Yuan, Y. Zhu, X. Zhang, J. Yan, Q. Jiang, P3-type $K_{0.33}Co_{0.53}Mn_{0.47}O_2{\cdot}0.39H_2O$: a novel bifunctional electrode for Na-ion batteries, Mater. Horiz. 4 (2017) 1122–1127.
[11] S. Wang, S. Yuan, Y.B. Yin, Y.H. Zhu, X.B. Zhang, J.M. Yan, Green and facile fabrication of MWNTs@Sb2S3@PPy coaxial nanocables for high-performance Na-ion batteries, Part. Part. Syst. Char. 33 (2016) 493–499.
[12] W. Yao, J. Chen, L. Zhan, Y. Wang, S. Yang, Two-dimensional porous sandwich-like C/Si-graphene-Si/C nanosheets for superior lithium storage, ACS Appl. Mater. Interfaces 9 (2017) 39371–39379.
[13] Q. Liu, W. Yao, L. Zhan, Y. Wang, Y. Zhu, V_3S_4 nanoparticles anchored on three-dimensional porous graphene gel for superior lithium storage, Electrochim. Acta 261 (2018) 35–41.
[14] J. Leng, H. Mei, L. Zhan, Y. Wang, S. Yang, Y. Song, V_2O_3 nanoparticles anchored onto the reduced graphene oxide for superior lithium storage, Electrochim. Acta 231 (2017) 732–738.
[15] S. Dong, L. Shen, H. Li, G. Pang, H. Dou, X. Zhang, Flexible sodium-ion pseudo-capacitors based on 3D $Na_2Ti_3O_7$ nanosheet arrays/carbon textiles anodes, Adv. Funct. Mater. 26 (2016) 3703–3710.
[16] J. Ding, H. Wang, Z. Li, K. Cui, D. Karpuzov, X. Tan, A. Kohandehghan, D. Mitlin, Peanut shell hybrid sodium ion capacitor with extreme energy-power rivals lithium ion capacitors, Energy Environ. Sci. 8 (2015) 941–955.
[17] M.M. Doeff, M.Y. Peng, Y. Ma, L.C. De Jonghe, Orthorhombic Na_xMnO_2 as a cathode material for secondary sodium and lithium polymer batteries, J. Electrochem. Soc. 141 (1994) L145–L147.
[18] A. Abouimrane, W. Weng, H. Eltayeb, Y. Cui, J. Niklas, O. Poluektov, K. Amine, Sodium insertion in carboxylate based materials and their application in 3.6 V full sodium cells, Energy Environ. Sci. 5 (2012) 9632–9638.
[19] B.L. Ellis, W.R.M. Makahnouk, Y. Makimura, K. Toghill, L.F. Nazar, A multi-functional 3.5 V iron-based phosphate cathode for rechargeable batteries, Nat. Mater. 6 (2007) 749–753.
[20] J.J. Braconnier, C. Delmas, C. Fouassier, P. Hagenmuller, Comportement electro-chimique des phases Na_xCoO_2, Mater. Res. Bull. 15 (1980) 1797–1804.
[21] J.M. Paulsen, J.R. Dahn, Studies of the layered manganese bronzes, $Na_{2/3}[Mn_{1-x}M_x]O_2$ with M = Co, Ni, Li, and $Li_{2/3}[Mn_{1-x}M_x]O_2$ prepared by ion-exchange, Solid State Ionics 126 (1999) 3–24.
[22] P. Moreau, D. Guyomard, J. Gaubicher, F. Boucher, Structure and stability of sodium intercalated phases in olivine $FePO_4$, Chem. Mater. 22 (2010) 4126–4128.
[23] M.D. Slater, D. Kim, E. Lee, C.S. Johnson, Sodium-ion batteries, Adv. Funct. Mater. 23 (2013) 947–958.
[24] R. Alcántara, M. Jaraba, P. Lavela, J.L. Tirado, $NiCo_2O_4$ spinel: first report on a transition metal oxide for the negative electrode of sodium-ion batteries, Chem. Mater. 14 (2002) 2847–2848.
[25] H. Xiong, M.D. Slater, M. Balasubramanian, C.S. Johnson, T. Rajh, Amorphous TiO_2 nanotube anode for rechargeable sodium ion batteries, J. Phys. Chem. Lett. 2 (2011) 2560–2565.
[26] P. Senguttuvan, G. Rousse, V. Seznec, J.M. Tarascon, M.R. Palacín, $Na_2Ti_3O_7$: lowest voltage ever reported oxide insertion electrode for sodium ion batteries, Chem. Mater. 23 (2011) 4109–4111.
[27] Y. Wang, X. Yu, S. Xu, J. Bai, R. Xiao, Y.S. Hu, H. Li, X.Q. Yang, L. Chen, X. Huang, A zero-strain layered metal oxide as the negative electrode for long-life sodium-ion batteries, Nat. Commun. 4 (2013) 2365.
[28] Y. Jiang, M. Hu, D. Zhang, T. Yuan, W. Sun, B. Xu, M. Yan, Transition metal oxides for high performance sodium ion battery anodes, Nanomater. Energy 5 (2014) 60–66.
[29] H. Banda, D. Damien, K. Nagarajan, A. Raj, M. Hariharan, M.M. Shaijumon, Twisted perylene diimides with tunable redox properties for organic sodium-ion batteries, Adv. Energy Mater 7 (2017) 1701316.
[30] Q. Zhao, Y. Lu, J. Chen, Advanced organic electrode materials for rechargeable sodium-ion batteries, Adv. Energy Mater 7 (2017) 1601792.
[31] Z. Song, H. Zhou, Towards sustainable and versatile energy storage devices: an overview of organic electrode materials, Energy Environ. Sci. 6 (2013) 2280–2301.
[32] H. Wu, K. Wang, Y. Meng, K. Lu, Z. Wei, An organic cathode material based on a polyimide/CNT nanocomposite for lithium ion batteries, J. Mater. Chem. A 1 (2013) 6366–6372.
[33] A. Iordache, V. Delhorbe, M. Bardet, L. Dubois, T. Gutel, L. Picard, Perylene-based all-organic redox battery with excellent cycling stability, ACS Appl. Mater. Interfaces 8 (2016) 22762–22767.
[34] M. Lee, J. Hong, J. Lopez, Y. Sun, D. Feng, K. Lim, W.C. Chueh, M.F. Toney, Y. Cui, Z. Bao, High-performance sodium-organic battery by realizing four-sodium storage in disodium rhodizonate, Nature Energy 2 (2017) 861–868.
[35] M.K. Ghosh, K.L. Mittal, Polyimides: Fundamentals and Applications, Marcel Dekker, New York, 1996.
[36] B. Häupler, A. Wild, U.S. Schubert, Carbonyls: powerful organic materials for secondary batteries, Adv. Energy Mater 5 (2015) 1402034.
[37] J.M. Seo, S.J. Kim, H. Chung, E.T. Kim, H.G. Yu, Y.S. Yu, Biocompatibility of polyimide microelectrode array for retinal stimulation, Mater. Sci. Eng. C 24 (2004) 185–189.
[38] W. Luo, M. Allen, V. Raju, X. Ji, An organic pigment as a high-performance cathode for sodium-ion batteries, Adv. Energy Mater 4 (2014) 1400554.
[39] H. Wang, S. Yuan, D. Ma, X. Huang, F. Meng, X. Zhang, Tailored aromatic carbonyl derivative polyimides for high-power and long-cycle sodium-organic batteries, Adv. Energy Mater 4 (2014) 1301651.
[40] F. Xu, J. Xia, W. Shi, Anthraquinone-based polyimide cathodes for sodium secondary batteries, Electrochem. Commun. 60 (2015) 117–120.
[41] H. Banda, D. Damien, K. Nagarajan, M. Hariharan, M.M. Shaijumon, A polyimide based all-organic sodium ion battery, J. Mater. Chem. A 3 (2015) 10453–10458.
[42] Z. Song, H. Zhan, Y. Zhou, Polyimides: promising energy-storage materials, Angew. Chem. Int. Ed. 122 (2010) 8622–8626.
[43] D.H. Zhong, H. Sano, Y. Uchiyama, K. Kobayashi, Effect of low-level boron doping on oxidation behavior of polyimide-derived carbon films, Carbon 38 (2000) 1199–1206.
[44] M. Inagaki, T. Morishita, A. Kuno, T. Kito, M. Hirano, T. Suwa, K. Kusakawa, Carbon foams prepared from polyimide using urethane foam template, Carbon 42 (2004) 497–502.
[45] S. Wang, L. Xia, L. Yu, L. Zhang, H. Wang, X.W. Lou, Free-standing nitrogen-doped carbon nanofiber films: integrated electrodes for sodium-ion batteries with ultra-long cycle Life and superior rate capability, Adv. Energy Mater 6 (2016) 1502217.
[46] Q. Zhao, R.R. Gaddam, D. Yang, E. Strounina, A.K. Whittaker, X.S. Zhao, Pyromellitic dianhydride-based polyimide anodes for sodium-ion batteries, Electrochim. Acta 265 (2018) 702–708.
[47] F. Deng, L. Yu, G. Cheng, T. Lin, M. Sun, F. Ye, Y. Li, Synthesis of ultrathin mesoporous $NiCo_2O_4$ nanosheets on carbon fiber paper as integrated high-performance electrodes for supercapacitors, J. Power Sources 251 (2014) 202–207.
[48] Q. An, Q. Wei, L. Mai, J. Fei, X. Xu, Y. Zhao, M. Yan, P. Zhang, S. Huang, Supercritically exfoliated ultrathin vanadium pentoxide nanosheets with high rate capability for lithium batteries, Phys. Chem. Chem. Phys. 15 (2013) 16828–16833.
[49] Alar Jänes, Heisi Kurig, Enn Lust, Characterisation of activated nanoporous carbon for supercapacitor electrode materials, Carbon 45 (2007) 1226–1233.
[50] Q. Zhao, X. Wang, J. Liu, H. Wang, Y. Zhang, J. Gao, Q. Lu, H. Zhou, Design and synthesis of three-dimensional hierarchical ordered porous carbons for super-capacitors, Electrochim. Acta 154 (2015) 110–118.
[51] B. Daffos, P.L. Taberna, Y. Gogotsi, P. Simon, Recent advances in understanding the capacitive storage in microporous carbons, Fuel Cells 10 (2010) 819–824.
[52] H. Kim, M.E. Fortunato, H. Xu, J.H. Bang, K.S. Suslick, Carbon microspheres as supercapacitors, J. Phys. Chem. C 115 (2011) 20481–20486.
[53] M. Zhou, F. Pu, Z. Wang, S. Guan, Nitrogen-doped porous carbons through KOH activation with superior performance in supercapacitors, Carbon 68 (2014) 185–194.
[54] M. Yang, Y. Zhong, J. Bao, X. Zhou, J. Wei, Z. Zhou, Achieving battery-level energy density by constructing aqueous carbonaceous supercapacitors with hierarchical porous N-rich carbon materials, J. Mater. Chem. A 3 (2015) 11387–11394.
[55] Z. Xing, Z. Ju, Y. Zhao, J. Wan, Y. Zhu, Y. Qiang, Y. Qian, One-pot hydrothermal synthesis of Nitrogen-doped graphene as high-performance anode materials for lithium ion batteries, Sci. Rep. 6 (2016) 26146.
[56] Y. Shao, J. Xiao, W. Wang, M. Engelhard, X. Chen, Z. Nie, M. Gu, L.V. Saraf, G. Exarhos, J.G. Zhang, J. Liu, Surface-driven sodium ion energy storage in nanocellular carbon foams, Nano Lett. 13 (2013) 3909–3914.
[57] H. Kim, Y.U. Park, K.Y. Park, H.D. Lim, J. Hong, K. Kang, Novel transition-metal-free cathode for high energy and power sodium rechargeable batteries, Nanomater. Energy 4 (2014) 97–104.
[58] H. Wang, Y. Zhang, H. Ang, Y. Zhang, H.T. Tan, Y. Zhang, Y. Guo, J.B. Franklin, X.L. Wu, M. Srinivasan, H.J. Fan, Q. Yan, A high-energy lithium-ion capacitor by integration of a 3D interconnected titanium carbide nanoparticle chain anode with a pyridine-derived porous nitrogen-doped carbon cathode, Adv. Funct. Mater. 26 (2016) 3082–3093.
[59] J. Ding, H. Zhou, H. Zhang, T. Stephenson, Z. Li, D. Karpuzov, D. Mitlin, Exceptional energy and new insight with a sodium-selenium battery based on a carbon nanosheet cathode and a pseudographite anode, Energy Environ. Sci. 10 (2017) 153–165.
[60] Z. Le, F. Liu, P. Nie, X. Li, X. Liu, Z. Bian, G. Chen, H.B. Wu, Y. Lu, Pseudocapacitive sodium storage in mesoporous single-crystal-like TiO_2-graphene nanocomposite enables high-performance sodium-ion capacitors, ACS Nano 11 (2017) 2952–2960.
[61] S. Mai, M. Xu, X. Liao, J. Hu, H. Lin, L. Xing, Y. Liao, X. Li, W. Li, Tris(trimethylsilyl) phosphite as electrolyte additive for high voltage layered lithium nickel cobalt manganese oxide cathode of lithium ion battery, Electrochim. Acta 147 (2014) 565–571.
[62] E. Endo, T. Yasuda, A. Kita, K. Yamaura, K. Sekai, A $LiCoO_2$ cathode modified by plasma chemical vapor deposition for higher voltage performance, J. Electrochem. Soc. 147 (2000) 1291–1294.
[63] J. Yin, L. Qi, H. Wang, Sodium titanate nanotubes as negative electrode materials for sodium-ion capacitors, ACS Appl. Mater. Interfaces 4 (2012) 2762–2768.
[64] Z. Chen, V. Augustyn, X. Jia, Q. Xiao, B. Dunn, Y. Lu, High-performance sodium-ion pseudocapacitors based on hierarchically porous nanowire composites, ACS Nano 6 (2012) 4319–4327.
[65] R. Ding, L. Qi, H. Wang, An investigation of spinel $NiCo_2O_4$ as anode for Na-ion capacitors, Electrochim. Acta 114 (2013) 726–735.
[66] H. Li, Y. Zhu, S. Dong, L. Shen, Z. Chen, X. Zhang, G. Yu, Self-assembled Nb_2O_5 nanosheets for high energy-high power sodium ion capacitors, Chem. Mater. 28 (2016) 5753–5760.
[67] Z. Jian, V. Raju, Z. Li, Z. Xing, Y.S. Hu, X. Ji, A high-power symmetric Na-ion pseudocapacitor, Adv. Funct. Mater. 25 (2015) 5778–5785.